# Practical Method to Limit Tip−Sample Contact Stress and Prevent Wear in Amplitude Modulation Atomic Force Microscopy

Vahid Vahdat and Robert W. Carpick[*]

Department of Mechanical Engineering and Applied Mechanics, University of Pennsylvania, Philadelphia, Pennsylvania 19104, United States

ABSTRACT Amplitude modulation atomic force microscopy (AM-AFM) is one of the most popular AFM modes because of the reduced tip−sample interaction, compared to contact mode AFM, and the ability to acquire high-resolution images while interrogating the sample's material composition through phase imaging. Despite the reduced tip−sample interaction, tip and sample wear can occur through gradual atomic scale processes that can significantly accumulate due to the high frequency of the tip−sample interaction and through high intermittent contact stresses. Starting from existing analytical formulations, we introduce a method for selecting an appropriate probe and free oscillation amplitude that avoids exceeding a critical contact stress to minimize tip/

sample damage. The approach is presented for the case of both a Hertzian- and a Derjaguin−Müller−Toporov-like tip−sample contact. Stress maps and related simplified formulas are provided that enable one to determine allowable free oscillation amplitudes to stay below a target contact stress for given cantilever and sample parameters (combined into a single "cantilever−sample constant" that we introduce). Experimental results show how sharp silicon tips, either uncoated or coated with diamond-like carbon and silicon nitride, interacting with a hard and wear-resistant sample (ultrananocrystalline diamond) can be preserved while attaining high-quality AM-AFM images by using our proposed scheme. We also show that using our analysis to select parameters that exceed the target contact stress indeed leads to significant tip wear. This method provides AM-AFM users with a better understanding of contact stresses and enables selection of AM-AFM cantilevers and experimental parameters that preserve the tip for long periods of use and prevents the sample from damage.
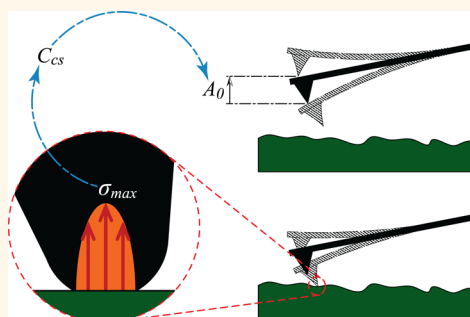
KEYWORDS: atomic-scale wear · AM-AFM · amplitude modulation · tapping mode · peak repulsive force · contact stress · contact mechanics

A mplitude modulation atomic force microscopy (AM-AFM, also known as tapping mode AFM) is a method of choice for many AFM users because of the small and controlled interaction of the tip and sample, which if utilized appropriately greatly reduces tip/sample wear and deformation compared to contact mode schemes. For the same reason, AM-AFM is used for metrology purposes by the micro/nanoelectromechanical systems industry[1] and for imaging soft materials such as biological samples without damaging them.[2,3] Nanoscale lithography, patterning, manipulation, and surface characterization are some of the other common applications of AM-AFM.[4−8] However, the advantage of minimizing

the tip−sample interaction in AM-AFM compared to contact mode AFM can be lost if one selects experimental settings that result in the contact stresses beyond the tip/sample material's yield/failure stress. Particularly important parameters are the free oscillation amplitude, A_0, or the amplitude ratio, A_{ratio}, which is the tapping amplitude while interacting with the sample divided by free oscillation amplitude. High contact stresses and associated tip or sample wear can readily occur, as it can be challenging to fully understand the complex mechanics and dynamics of the nonlinear tip−sample interactions. Consequently, one may fail to appropriately control the experimental parameters to ensure that contact stresses

are sufficiently low to prevent failure of the tip or undesirable wear of the sample.

At the nanoscale, there are three primary wear mechanisms that have been identified: fracture,[9,10] plastic deformation,[11] and atom-by-atom removal.[12−14] All of these mechanisms could occur in both contact mode and AM-AFM. However, how these mechanisms occur and which one dominates strongly depend on the stress state and the nature of the tip−sample interactions at the contact. In contact mode, tip wear occurs during sliding and is influenced by the magnitude of the stresses in the contact, potentially by shear stresses. The causes of wear in AM-AFM can be quite different. While interfacial shear stresses are significantly reduced, the effects of cyclic loading and impact, uniquely related to repeated contact formation and breakage of AM-AFM, and the potential for excursions to high compressive stresses may lead to distinct types of wear processes compared with contact mode AFM.

There have been numerous analytical and numerical studies on the dynamics of AM-AFM and the forces that act on the tip and sample.[2,15−21] There are few studies that propose particular experimental settings to reduce or prevent damage to the tip and sample while operating in AM-AFM mode; however, most of them are limited to a particular tip and sample material or imaging conditions.[22−25]

In a study by Tello et al.,[22] it was demonstrated that during repeated imaging of cobalt nanoparticles in attractive mode/soft tapping, in which attractive forces are dominant,[2,16] the apparent height and width of the nanoparticles were constant. However, imaging in repulsive mode/hard tapping, in which repulsive forces are dominant, permanently changed their height. Although in this study the contact forces and stresses in the repulsive regime were not specifically controlled to avoid sample damage, it confirms that forces in attractive regime are not significant enough to cause permanent deformation. San Paulo et al.[23] made similar conclusions through imaging antibodies.

However, there are several issues that make imaging in attractive regime either impossible or undesirable. In a lot of cases, depending on the tip and sample elastic properties, the cantilever's physical properties, and the AM-AFM experimental settings, the range of amplitude ratios where stable attractive mode imaging is possible (where attractive forces dominate repulsive forces) is very limited. Sometimes a stable attractive regime does not exist at all, and the tip−sample interaction jumps into the repulsive mode as soon as the interaction begins. This short-range of amplitude ratios makes stable imaging (i.e., effectively tracking the sample features and avoiding bistability[2]) very difficult. In cases where there is a wide range of amplitude ratios available in the attractive regime, tip broadening[26] (i.e., showing features wider than their real size because of

the fact that attractive forces are long-range) or loss of tracking of the surface can make attractive imaging undesirable or challenging. Loss of tracking of the surface can cause image artifacts and uncontrolled impact of the tip with the surface, resulting in tip or surface damage.[25] This problem arises from the fact that the transient time for the amplitude error to reach equilibrium exponentially increases as the amplitude ratio approaches 1, which is the range where attractive-mode imaging needs to be performed. Whenever there is a transient component in the amplitude error, it can be falsely interpreted as sample features, resulting in the feedback system losing track of the surface.[25]

Su et al.[25] showed that imaging in repulsive mode with a relatively low amplitude ratio has the advantage of reducing tip wear and allowing the scanning speed to be increased, in contrast to operating with a high amplitude ratio. They also found that by decreasing the amplitude ratio, the interaction force goes through a maximum and then decreases as the low amplitude ratio is approached. This implies that an amplitude ratio of 0.4 to 0.5 is the most damaging condition, and they calculate that at this point the tapping velocity is at a maximum value. This work sheds light on some of the experimental parameters affecting tip wear. However, a general quantitative analysis that takes into account all the experimental parameters as well as the cantilever properties and the tip's and sample's physical and material properties has not yet been presented.

Here, we introduce analytical expressions for determining the tip−sample forces and stresses over a wide range of AM-AFM experimental parameters and tip and sample materials, in ambient condition. We then combine and simplify these expressions for two purposes. First, the simpler closed-form equation allows one to easily choose a safe free oscillation amplitude, which is the most critical parameter controlling tip/sample wear. Second, this simplification is used to plot stress maps. These maps reveal the expected range of contact stresses for a given cantilever and sample, guiding one in choosing the appropriate probe for a particular AM-AFM experiment (based on assumptions of continuum contact mechanics). The approach is examined experimentally by scanning a stiff and wear-resistant sample, ultrananocrystalline diamond (UNCD), using a bare silicon probe and silicon probes coated with diamond-like carbon (DLC) and silicon nitride (SiN$_x$), two common materials used to coat AFM probes to increase their wear resistance.

RESULTS AND DISCUSSION

Mapping Stress. There are several important assumptions used to develop the analytical expressions that will be presented in the next section. First, we assume that the tip−sample contact is either Hertzian-[27] or Derjaguin−Müller−Toporov (DMT)[28]-like. In a DMT-like contact, the normal contact stress distribution is

identical to that of the Hertz theory but at a higher load, due to adhesion. Thus, adhesion between the tip and sample increases the stresses and the contact area beyond the Hertz prediction. Also, in a DMT-like contact, the contact area and stresses are nonzero at zero applied load. The reason for considering Hertzian and DMT-like contact here is the availability of closed-form equations to estimate peak repulsive force (the maximum repulsive force in an oscillation cycle) that is presented later.

If the contact cannot be described by the Hertz or DMT contact mechanics model, the results here will not be accurate and one should seek other means such as the virtual environment for dynamic AFM (VEDA)[29] provided by http://nanohub.org to calculate relevant forces. Determination of which contact mechanics model suits a particular tip–sample ensemble is described in detail in the literature.[21,30,31]

Second, we choose the failure criterion in AM-AFM to correspond to the case where the maximum compressive contact stress experienced during AM-AFM cyclic operation is equal to the yield stress (which could also be chosen to be any other desired failure stress) of the tip or sample material, whichever is smaller. The motivation for selecting this criterion in a Hertzian or DMT contact is discussed in detail in the Methods section.

Another important assumption is the absence of any capillary formation between the tip and sample. Capillary formation alters the value of the peak repulsive force from what is calculated here. There are multiple studies discussing the effect of capillary formation in AM-AFM that can be used to account for the additional stresses caused by the formation of a capillary. Through friction force microscopy, it has been shown that the time required for capillary meniscus nucleation between the tip and sample at 40% relative humidity (RH) can be on the order of a few milliseconds.[32] However, in typical AM-AFM experiments, the contact time is on the order of a few microseconds; in the experiments performed here, contact time ranges from 0.1 to 0.5 μs. Because of the short contact times and the strong dependence of water condensation on RH,[33] Sahagún et al.[34] concluded that in AM-AFM capillary bridges form only when the RH exceeds 50%.

In another study, Zitzler et al.[35] did not observe any significant change in the transition from attractive to repulsive regimes across a wide range of RH, from 3% to 96%, when using AM-AFM on a hydrophobic sample. This finding implies that, in the case of hydrophobic samples, capillary formation does not influence AM-AFM operation. However, Zitzler et al. observed a moderate change in the transition from attractive to repulsive regimes between 30% and 70% RH and a significant change above ~70% RH, where the tip

and sample were both hydrophilic. To summarize the conclusions of these two studies, capillary forces can be ignored when determining tip–sample forces if the RH is below 40% or the sample is hydrophobic. In other cases where capillary formation is significant, one must use VEDA to include capillary formation in the calculation of the peak repulsive force. All the experiments in this work are performed in a mixture of humid air and dry nitrogen gas with 15% RH. Therefore, the capillary forces are not considered in our estimation of forces and stresses.

It is important to note that the effect of adsorbates (including a thin water layer in the case of hydrophilic tip or sample materials and/or other contaminants) on the tip–sample contact and the ensuing wear processes is not accounted for here. Despite this, our approach to reduce/eliminate wear through limiting the contact stress works rather well for the cases tested, as seen in the Experimental Results section. The influence of such adsorbates should be assessed in future studies.

Finally, the analysis and methods presented here apply to AM-AFM imaging with scanning velocities less than 100 μm/s. Under these conditions, the amount of lateral sliding that takes place while the tip is in contact with the sample due to scanning is negligible, less than an atomic bond length. As a consequence, abrasive wear is unlikely to contribute to wear in typical AM-AFM. In contrast, for scanning velocities greater than 100 μm/s, which fall into the category of high-speed AM-AFM imaging, the relative lateral tip–sample displacement during the contact time and the corresponding shear stresses may be significant, resulting in different wear mechanisms. Under these assumptions, we consider the Hertzian- and DMT-like contacts separately in the following sections.

Peak Repulsive Force: Assumptions and Dependence on Amplitude Ratio. An AM-AFM experiment involves two distinctive steps: approaching the sample and then scanning it. Before approaching the sample, the primary flexural resonance frequency of the cantilever is determined. The cantilever is then excited at a fixed drive frequency at or near this measured resonance frequency. Subsequently, the sample is brought closer to the tip, through moving either the sample up or the probe chip down. As the approach continues, the oscillation amplitude decreases as a consequence of the shift in resonance frequency and increased damping. Both the shift in the cantilever resonant frequency and increased damping result from the tip–sample interaction. This reduction continues until the oscillation amplitude reaches a predetermined value, usually referred to as the set point amplitude/tapping amplitude, defined by the user. After reaching the target amplitude, in the second step of the AM-AFM experiment, the raster scanning of the sample begins. While

scanning a surface, the oscillation amplitude tends to change as a result of interacting with topographic features. The AFM feedback loop monitors the oscillation amplitude and keeps it constant by adjusting the height of the sample continuously. The quality of the image, as well as the precision with which the amplitude set point is maintained, is therefore determined by the feedback loop.

During an oscillation cycle, as the tip approaches and then retracts from a surface, it experiences two different force regimes: when far from the sample's surface, the tip experiences long-range attractive forces, mainly as a result of the van der Waals interaction with the sample; when close to the sample's surface, the tip experiences short-range repulsive forces as a result of Pauli and electrostatic repulsion, and strong short-range attractive forces as a result of metallic, covalent, ionic, or hydrogen-bonding interactions, for example. Capillary interactions can also contribute to attractive forces over intermediate separation ranges. The maximum repulsive (i.e., normal) force is experienced by the tip during contact when it reaches its farthest distance away from its equilibrium position (i.e., cantilever rest position), which corresponds to the closest tip−sample distance in a tapping cycle. This peak repulsive force is denoted by F_{peak}^{rep}. Finally, the cantilever begins to pull the tip away from the sample. Then, the same sequence of the tip−sample force regimes are passed through in reverse.

Through applying a nonlinear dynamics method to the point-mass spring model of a driven AFM cantilever interacting with sample and some mathematical approximations, Hu et al.[36] proposed the following expression, which is accurate over a wide range of experimental settings and physical parameters under ambient conditions, to calculate peak repulsive force in the case of DMT-like contact:

$$F_{peak}^{rep} \approx 2^{1/8} 3^{-1/4} \pi^{3/4} (E*\sqrt{R})^{1/4} \left(\frac{k}{Q}\right)^{3/4} A_0^{9/8} A_{ratio}^{9/8}$$

$$\times \left\{ (-1+\Omega^2)Q + \sqrt{\frac{1}{A_{ratio}^2}[\Omega^2 + (1-\Omega^2)^2 Q^2] - \Omega^2} \right\}^{3/4}$$

$$- F_{adhesion}/2 \quad \text{where} \quad \frac{1}{E*} = \frac{(1-\nu_t^2)}{E_t} + \frac{(1-\nu_s^2)}{E_s}$$

$$\text{and} \quad F_{adhesion} = -2\pi wR \qquad (1)$$

where $E*$ is the reduced Young's modulus, R is the tip radius, k is the cantilever spring constant, Q is the cantilever's quality factor for the primary flexural mode, Ω is drive frequency divided by the resonance frequency of the cantilever's primary flexural mode, $F_{adhesion}$ is the adhesion force, E_t and E_s are Young's moduli for the tip and sample, ν_t and ν_s are Poisson's ratios for the tip and sample, and w is the work of adhesion. Equation 1 is valid for both attractive and repulsive mode imaging. Therefore, the
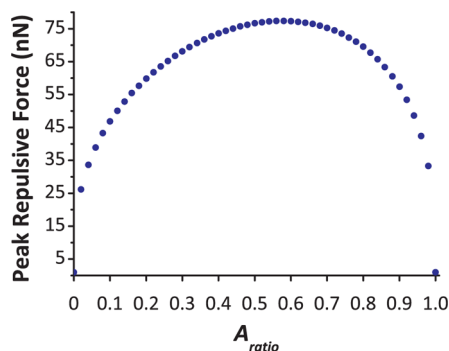

Figure 1. Peak repulsive force as a function of amplitude ratio for a cantilever with a spring constant of 40 N/m, quality factor of 400, tip radius of 10 nm, free oscillation amplitude of 50 nm, reduced Young's modulus of 70 GPa, and work of adhesion of 30 mJ/m².

methods presented in the following sections to control contact stress and prevent wear are valid for both imaging modes. As a consequence, users do not need to aim for imaging in the attractive or repulsive regime, as proposed by other investigators, to prevent tip wear[25] or sample deformation.[22,23]

If one plots the peak repulsive force as a function of the amplitude ratio using eq 1, it can be seen that as the cantilever carrier chip approaches the sample and consequently the amplitude ratio decreases, the peak repulsive force increases until it reaches a maximum value. If the approach continues beyond this point, the tip−sample repulsive force is reduced, despite a common misconception among users who generalize that a further reduction in oscillation amplitude suggests increased repulsive forces. To illustrate this, an example is shown in Figure 1, where experimentally reasonable values are chosen for the various parameters. The approximate amplitude ratio, where the peak repulsive force reaches its maximum value, is an important parameter to take into account in the following calculations to estimate the maximum possible compressive stress.

Hertzian Contact: In this section, we simplify the analytical expressions governing the tip−sample interaction by combining and nondimensionalizing them and plotting them in a manner useful to choose appropriate cantilever and experimental settings to control maximum compressive stress.

Nondimensionalization of the Maximum Compressive Stress: If the contact follows Hertzian behavior, the adhesion force is ignored. Therefore, we just use the first term of eq 1 to calculate the peak repulsive force. In a Hertzian contact, the maximum normal stress is located at the center of contact and can be calculated through

$$\sigma_{max} = \frac{3}{2\pi} \left(\frac{4E*}{3R}\right)^{2/3} F_{total}^{1/3} \qquad (2)$$

where $F_{total} = F_{peak}^{rep}$. By plugging eq 1 with $F_{adhesion} = 0$ into eq 2 and rearranging the parameters, we obtain

$$\tilde{\sigma} \approx 0.723 \left(\frac{A_0 A_{ratio}}{C_{cs}} \right)^{3/8}$$

$$\times \left\{ (-1 + \Omega^2)Q + \sqrt{\frac{1}{A_{ratio}^2}[\Omega^2 + (-1+\Omega^2)^2 Q^2] - \Omega^2} \right\}^{1/4}$$

$$\text{where} \quad \tilde{\sigma} = \frac{\sigma_{max}}{E^*} \text{ and } C_{cs} = \left(\frac{E^* Q}{k} \right)^{2/3} R^{5/3} \quad (3)$$

Equation 3 is in nondimensionalized format. The parameter C_{cs}, which we call the "cantilever–sample constant", is critical for minimizing tip/sample damage by choosing the correct cantilever properties and experimental settings for AM-AFM experiments. It should be mentioned that C_{cs} is not dimensionless, having units of nm, as k is in N/m, E^* is in GPa, and R is in nm. Also, C_{cs} is primarily defined by the physical properties of the cantilever (k, Q, R), although it includes information regarding the tip and sample material's Young's modulus and Poisson's ratio through the parameter E^*.

As mentioned previously, there is a particular A_{ratio} at which the peak repulsive force reaches its maximum value as the tip approaches the sample. This situation can be avoided by operating with larger A_{ratio} values; otherwise, if the cantilever is operated below this critical A_{ratio} (which corresponds to a smaller peak force), the tip still has to pass through this ratio during the approach process. In other words, the tip will (briefly) experience the highest peak force and maximum stress transiently during approach and retraction, and this can exceed the tip's failure stress. Therefore, we consider the worst-case scenario, which is operating at this maximum peak force and contact stress for avoiding tip wear. This further simplifies the above nondimensionalized expression. From differentiating eq 1, the critical A_{ratio} is going to be equal to $1/\sqrt{3}$. By inserting this value into eq 3 and rearranging the equation, we obtain a maximum allowable value for the free oscillation amplitude:

$$A_0 \approx 4.109 C_{cs} \tilde{\sigma}^{8/3} \times \left\{ (-1 + \Omega^2)Q \right.$$

$$\left. + \sqrt{2\Omega^2 + 3(-1+\Omega^2)^2 Q^2} \right\}^{-2/3} \quad (4)$$

If we set Ω to 1, which applies when the drive frequency is equal to the resonance frequency, we can write

$$A_0 \approx 3.261 C_{cs} \tilde{\sigma}^{8/3} \quad (5)$$

Equation 4 or 5 can be used to quickly and accurately choose a free oscillation amplitude such that contact stresses are low enough to prevent tip/sample damage. To accomplish this, one would first choose the maximum compressive stress σ_{max} that is lower than the yield/failure stress of the tip or sample material, whichever is smaller. Second, the cantilever–sample

constant, C_{cs}, is calculated after determining the cantilever's resonance frequency, quality factor, spring constant, and tip radius through measurement or, if not possible, acquiring them from the manufacturer's specifications. The Young's modulus and Poisson's ratio of the material comprising the sample and the tip are also required in the determination of the C_{cs}, as stated before. Given the difficulty of measuring the tip radius, to maximize accuracy in determining C_{cs}, at least one should obtain measurements of the cantilever's resonance curve and spring constant.[37,38] This is important since the measured values for the cantilever resonance frequency and spring constant often deviate significantly from the manufacturer's specifications. The value of the tip radius is the most important among all the other parameters of C_{cs}, as it has the strongest dependence ($R^{5/3}$). As with the other specifications mentioned, the value of the tip radius provided by the manufacturer is not necessarily accurate. On the other hand, measuring the tip radius is very difficult and the instrumentation required to perform this measurement is not readily available to all users. Blind tip reconstruction (BTR), scanning electron microscopy, and transmission electron microscopy (TEM) are the methods that can be used to estimate the tip radius. Utilizing BTR and TEM to accurately estimate the tip radius of probes operating in AM-AFM is explained in detail by Vahdat et al.[21]

Stress Map for Hertzian Contact: We have created a map based on the above analysis that relates the maximum compressive stress, free oscillation amplitude, and C_{cs} using eq 5. This map can be easily consulted for determining the maximum allowable free oscillation amplitude for given cantilever properties and given tip and sample materials. The map is shown in Figure 2, where the variation of the free oscillation amplitude A_0 is plotted against the log of the maximum compressive stress normalized by the reduced Young's modulus ($\tilde{\sigma} = \sigma_{max}/E^*$) for various curves of constant C_{cs} values, which are written on their respective curves. To create a map with reasonable ranges, a variety of commercially available AFM probes that can be operated in AM-AFM mode are considered. Based on the cantilever specifications provided by several manufacturers and typical ranges of the elastic constants of various materials of interest, we determine two extreme limits for the calculated C_{cs}: one extreme dominates when tapping against a compliant sample, such as polystyrene ($E = 3$ GPa[39]), setting an approximate lower bound on the cantilever–sample constant; a second extreme occurs when tapping against a stiff sample, in this case diamond ($E = 1143$ GPa[40]), setting an upper bound. On the basis of these calculations, C_{cs} varies from 15 nm (corresponding to a silicon probe coated with chromium–gold from MikroMasch (HI'RES-C15/Cr–Au) tapping against polystyrene) to 3.6×10^6 nm (corresponding to a silicon probe coated with UNCD from Nanosensors (DT-FMR)
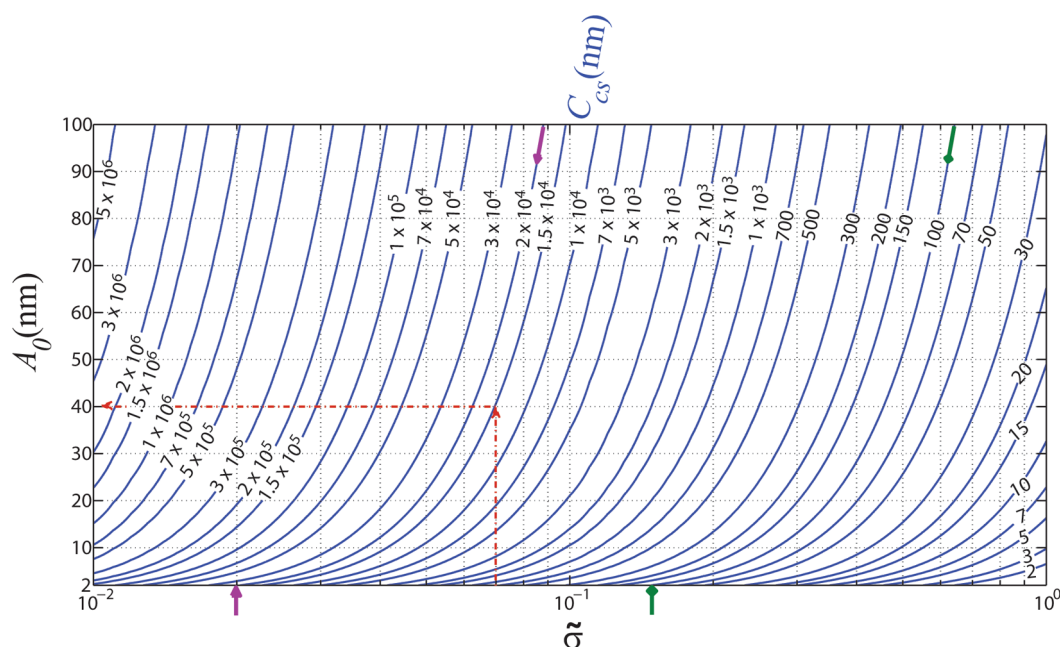
Figure 2. AM-AFM Hertzian contact stress map. The free oscillation amplitude A_0 is plotted against the log of the maximum compressive stress normalized by the reduced Young's modulus $\tilde{\sigma} = \sigma_{max}/E^*$ for a variety of cantilever−sample constants C_{cs} (values written on their respective curves) ranging from 2 to 5×10^6 nm. The vertical red dash-dotted arrow denotes the normalized maximum compressive stress used when imaging a silicon sample with a DLC-coated tip. The corresponding intersection point with the selected cantilever−sample constant curve ($C_{cs} = 1.5 \times 10^4$ nm) gives the maximum appropriate free oscillation amplitude permitted to avoid damaging the sample/tip during imaging, based on continuum mechanics. Green arrows with a diamond-shaped head indicate that the minimum achievable $\tilde{\sigma}$ using a cantilever with $C_{cs} = 100$ nm and a 2 nm free oscillation amplitude is 0.15. Magenta arrows with a triangular head indicate that the minimum achievable $\tilde{\sigma}$ using a cantilever with $C_{cs} = 2 \times 10^4$ nm and a 2 nm free oscillation amplitude is 0.02.

tapping against diamond). As can be seen, Figure 2 covers a wider range including values of the cantilever−sample constant ranging from 2 to 5×10^6 nm, beyond the values typical of commercially available probes, to demonstrate the stresses incurred at the extremes. The vertical axis, A_0, is chosen to range from 2 to 100 nm, which encompasses the most common values used in AM-AFM. In this map, the spring constant is in N/m, the tip radius and free oscillation amplitude are in nm, and the maximum compressive stress and reduced Young's modulus are in GPa.

Selection of the Cantilever and Free Oscillation Amplitude: As an example, Figure 2 is used here to determine safe free oscillation amplitudes when imaging a silicon sample with a DLC-coated probe from Mikro-Masch (HQ:XSC11/HARD, Lever D). The failure stress of silicon at compression varies from 5.0 to 9.0 GPa.[41] In this paper, we assume the midrange value of 7.0 GPa to be the failure stress of silicon at compression. The yield strength of DLC varies significantly depending on the deposition technique and composition. Gan *et al.*[42] reported a yield strength of 15 to 30 GPa for a DLC thin film deposited by filtered cathodic vacuum arc for example. These and other values for other desirable DLC coatings always exceed the failure stress of silicon. Therefore, the maximum stress, σ_{max}, should be chosen to be less than 7.0 GPa to avoid any damage to the silicon sample. The reduced Young's modulus of DLC against silicon (assuming $E_{si} = 130$ GPa, $\nu_{si} = 0.28$,

$E_{DLC} = 150$ GPa,[43] and $\nu_{DLC} = 0.3$[44]) is 76 GPa. Choosing $\tilde{\sigma} = \sigma_{max}/E^* = 0.07$ results in a $\sigma_{max} = 5.3$ GPa, which is less than the silicon yield strength and is safe to avoid sample and tip wear. The vertical arrow (red dash-dotted line) in Figure 2 corresponds to $\tilde{\sigma} = 0.07$. The cantilever−sample constant C_{cs} was then determined for the selected probe, which corresponds to approximately 1.5×10^4 nm. Given these two parameters, the free oscillation amplitude must be set equal to or less than 40 nm for imaging this particular sample with the selected tip. The horizontal arrow in Figure 2 indicates the location of the largest preferred amplitude.

From Figure 2, one can determine that any C_{cs}, which corresponds to a specific cantilever and sample, is effectively confined to a particular range of maximum compressive stresses. This is because of the instrumental limitations in achieving very small amplitudes, typically less than 2 to 3 nm, which sets a lower bound to the achievable maximum compressive stress. For example, if C_{cs} is approximately equal to 100 nm, corresponding to a particular experiment where a MikroMasch's HI'RES-C15 silicon cantilever coated with chromium−gold is used in an AM-AFM experiment examining a silicon sample, the lower bound for $\tilde{\sigma}$ is approximately 0.15 if the free oscillation amplitude is chosen to be 2 nm (green arrows with diamond-shaped head in Figure 2). This means the smallest possible σ_{max} is approximately 10.0 GPa. Given that gold is the outermost material on this particular

cantilever, we will assume its material properties in determining the reduced Young's modulus and whether or not the tip gets damaged. The ultimate tensile strength of the gold thin film at room temperature varies from 0.7 to 1.45 GPa.[45] Even though a very small free oscillation amplitude is chosen, the maximum compressive stress is larger than the ultimate tensile strength of the gold, predicting that tip wear will occur.

If instead one chooses MikroMasch's HQ:NSC19 silicon cantilever with no coating, it yields a corresponding C_{cs} of 2×10^4 nm, and consequently the $\tilde{\sigma}$ is then calculated to be 0.02 if the free oscillation amplitude is set at 2 nm (magenta arrows with triangular head in Figure 2). This means that the minimum achievable σ_{max} will be approximately 1.4 GPa, well below the silicon yield strength, and neither the tip nor the sample should be damaged. In fact, using this cantilever to examine the silicon sample, one can increase the free oscillation amplitude without predicting damage to the tip or sample to approximately 56 nm, which results in $\sigma_{max} \approx 5$ GPa.

Care should be taken, as all the calculations in this section are based on the assumption of Hertzian contact with no adhesion force. Tip−sample adhesion can significantly alter these results.

DMT-like Contact. *Nondimensionalization of the Maximum Compressive Stress:* The Hertzian approach discussed in the previous section does not include the effects of adhesion, which are often significant in nanoscale contacts. This section applies DMT contact mechanics to the calculations of the peak repulsive force and maximum compressive stress. Thus, the results account for the adhesive interactions in the limit of stiff, small-radii materials interacting *via* weak, long-range forces. Therefore, the second term in the expression for the peak repulsive force, eq 1, is not eliminated as it was in the case of Hertzian contact. Furthermore, the adhesion force must be added to the calculation of the maximum compressive stress in eq 2 and in the subsequent calculations. The maximum compressive stress then becomes

$$\sigma_{max} = \frac{3}{2\pi}\left(\frac{4E^*}{3R}\right)^{2/3}(F_{peak}^{rep} - F_{adhesion})^{1/3} \quad (6)$$

By plugging eq 1 into 6 and rearranging the parameters, we can write

$$\tilde{\sigma}' \approx 0.723\left(\frac{A_0 A_{ratio}}{C_{cs}}\right)^{3/8}\left\{(-1+\Omega^2)Q\right.$$
$$\left. + \sqrt{\frac{1}{A_{ratio}^2}[\Omega^2+(-1+\Omega^2)^2Q^2]-\Omega^2}\right\}^{1/4}$$
$$\text{where} \quad \tilde{\sigma}' = \left(\left(\frac{\sigma_{max}}{E^*}\right)^3 - \frac{18}{\pi^2}\left(\frac{w}{E^*R}\right)\right)^{1/3} \quad (7)$$

As with eq 3, eq 7 is in a nondimensionalized format. Similar to the Hertzian contact model discussed

earlier, the maximum possible compressive stress encountered during an AM-AFM experiment needs to be considered. This situation occurs when $A_{ratio} = 1/\sqrt{3}$. At this point, this amplitude ratio can be used to simplify and rearrange eq 7, so that we can write

$$A_0 \approx 4.109C_{cs}\tilde{\sigma}'^{8/3}\times\{(-1+\Omega^2)Q$$
$$+\sqrt{2\Omega^2+3(-1+\Omega^2)^2Q^2}\}^{-2/3} \quad (8)$$

If we set Ω to 1, which applies when the drive frequency is equal to the resonance frequency, we have

$$A_0 \approx 3.261C_{cs}\tilde{\sigma}'^{8/3} \quad (9)$$

It is interesting to notice that eqs 8 and 9, including their respective prefactors, are similar to eqs 4 and 5 in the case of the Hertzian contact. The only difference is the replacement of $\tilde{\sigma}$ in eqs 4 and 5 with $\tilde{\sigma}'$ in eqs 8 and 9, which includes the tip−sample work of adhesion. As with eqs 4 and 5 for nonadhesive contacts, eq 8 or 9 can be used to quickly and accurately choose a free oscillation amplitude such that tip/sample damage is prevented in the case of adhesive contacts. Similar to the procedure described before, the first step is to choose a maximum compressive stress that is lower than the yield/failure stress of the tip or sample material, whichever is smaller. Second, the tip−sample work of adhesion should be determined, *e.g.*, through pull-off force measurements or by estimation or reference to literature; one should err on the high side for the work of adhesion value in order to estimate the allowable amplitude, conservatively. It is then possible to determine the dimensionless parameter $\tilde{\sigma}'$ by combining the desired maximum compressive stress, tip−sample reduced Young's modulus, and work of adhesion *via* eq 7. Finally, the cantilever−sample constant C_{cs} should be calculated as before to be plugged into eq 8 or 9.

Stress Map for DMT-like Contact: Similar to Figure 2 in the case of Hertzian contact, Figure 3 shows the map that can be constructed to relate the $\tilde{\sigma}'$ value, free oscillation amplitude, and cantilever−sample constant using eq 9. The same range for C_{cs} (values ranging from 2 to 5×10^6 nm) is displayed in Figure 3, as was done in Figure 2. The range of C_{cs} corresponds to 2 orders of magnitude variation in $\tilde{\sigma}'$. The vertical axis, A_0, varies from 2 to 100 nm, again typical of most AM-AFM measurements. The spring constant is in N/m, the tip radius and free oscillation amplitude are in nm, the maximum normal compressive stress and reduced Young's modulus are in GPa, and the work of adhesion is in J/m^2.

Applying Figure 3 to select an appropriate cantilever and free oscillation amplitude can be performed in a similar way to that described for the Hertzian contact. Also, similar observations made from Figure 2 on the minimum achievable σ_{max} can be made here. Although Hertzian contact can be safely used for selection of an
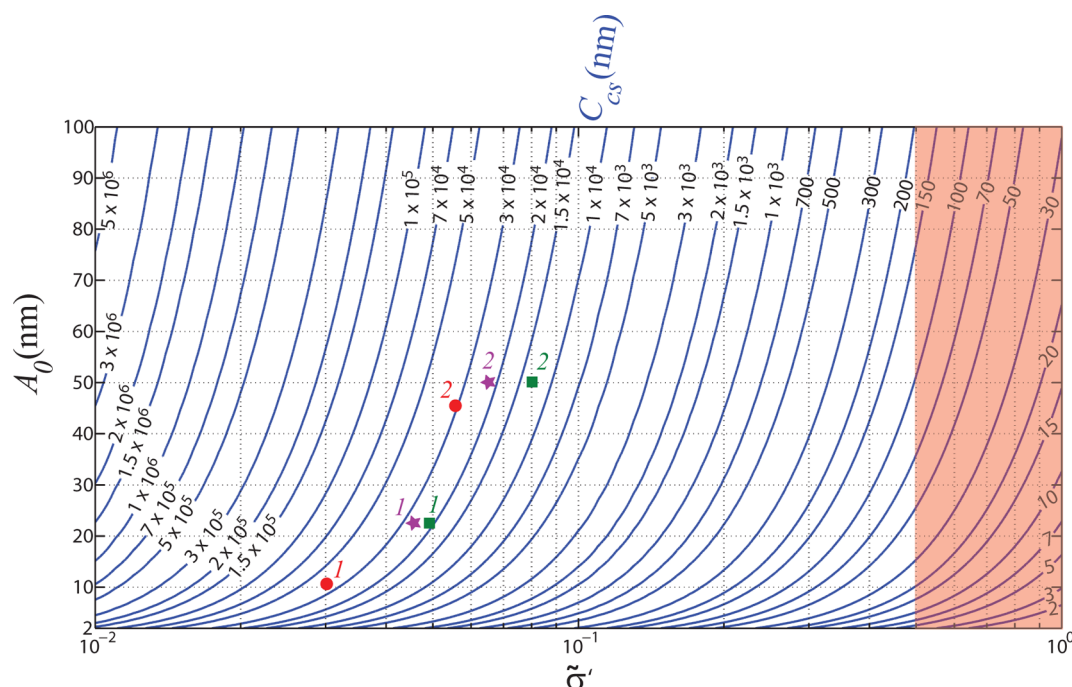
Figure 3. AM-AFM DMT-like contact stress map. The free oscillation amplitude is plotted against the dimensionless parameter $\tilde{\sigma}'$ for a variety of cantilever−sample constants ranging from 2 to 5×10^6 nm. The map can be used to choose appropriate cantilever and free oscillation amplitudes in a particular AM-AFM experiment to avoid tip/sample damage. The shaded area on the right corresponds to $\tilde{\sigma}'$ values greater than 0.5, where the DMT contact model does not hold and the use of this map will not be accurate. This is discussed in detail in the next section. The two red circles correspond to the initial $\tilde{\sigma}'$, C_{cs}, and A_0 values of the test sets 1 and 2 performed on the silicon probe. The two green squares correspond to the initial $\tilde{\sigma}'$, C_{cs}, and A_0 values of the DLC-coated tips 1 and 2. The two magenta stars correspond to that of the SiN_x-coated tips 1 and 2 discussed in the Experimental Results section.

appropriate cantilever and free oscillation amplitude if one chooses the maximum compressive stress conservatively such that it is well below the yield/fracture strength of the tip/sample, it is recommended to use the DMT-like approach, as adhesion can have considerable impact on the tip−sample forces and stresses.

As mentioned before, the appropriate contact mechanics model for a given tip and sample should be determined before using Figure 2 and Figure 3. In the following section, we approximate which regions of the Figure 3 might fall into the Maugis−Dugdale (M-D)[46] or Johnson−Kendall−Roberts (JKR)[47] contact regimes.

Determining the Limits of the DMT Contact Regime: To select the proper contact mechanics model, one needs to calculate the Maugis parameter λ and the nondimensional load $\bar{P}$ and then use the adhesion map proposed by Johnson and Greenwood.[31] The Maugis parameter λ and the nondimensional load $\bar{P}$ are calculated as follows:[31]

$$\lambda = 1.16 \left(\frac{Rw^2}{E^{*2}z_0^3} \right)^{1/3} \qquad (10)$$

$$\bar{P} = \frac{P}{\pi wR} \qquad (11)$$

where z_0 is the equilibrium separation and P is the total normal load, which here should be taken as

$F_{peak}^{rep} - F_{adhesion}$ (note that in ref 21 F_{peak}^{rep} was used instead; in fact this is not correct; the adhesion force should be included as well). Expressing the dimensionless parameter $\tilde{\sigma}'$ as a function of λ and $\bar{P}$ can help to determine which parts of the DMT-like contact stress map (Figure 3) might actually correspond to non-DMT contact regimes. By inserting eq 6 into the definition of $\tilde{\sigma}'$ in eq 7 and combining the resultant equation with eqs 10 and 11, $\tilde{\sigma}'$ can be rewritten as follows:

$$\tilde{\sigma}' = \left(\frac{6}{\pi^2}(\bar{P} - 3) \right)^{1/3} \left(\frac{z_0}{R} \right)^{1/2} \left(\frac{\lambda}{1.16} \right)^{1/2} \qquad (12)$$

In this analysis, we are going to assume that the net contact force at the bottom of the oscillation cycle is positive (repulsive). While it is possible to have a negative net force, wear is much less of a concern in this case. Therefore, we will only consider values of $\bar{P}$ greater than 3. This also ensures that the equations are used in a valid regime. Specifically, the smallest peak repulsive force allowed from eq 1 is πwR (this corresponds to $A_{ratio} = 1$). Inserting $F_{peak}^{rep} = \pi wR$ into eq 11, $\bar{P}$ becomes equal to 3. Note that smaller values of $\bar{P}$ are achievable in actual AM-AFM operation, but eq 1 is not valid in this case. Such a case corresponds to the peak repulsive force being less than πwR. We choose the upper limit of $\bar{P}$ to be 10^4 (note that in the adhesion map of Johnson and Greenwood,[31] $\bar{P}$ varies from 0.01 to 10^4).
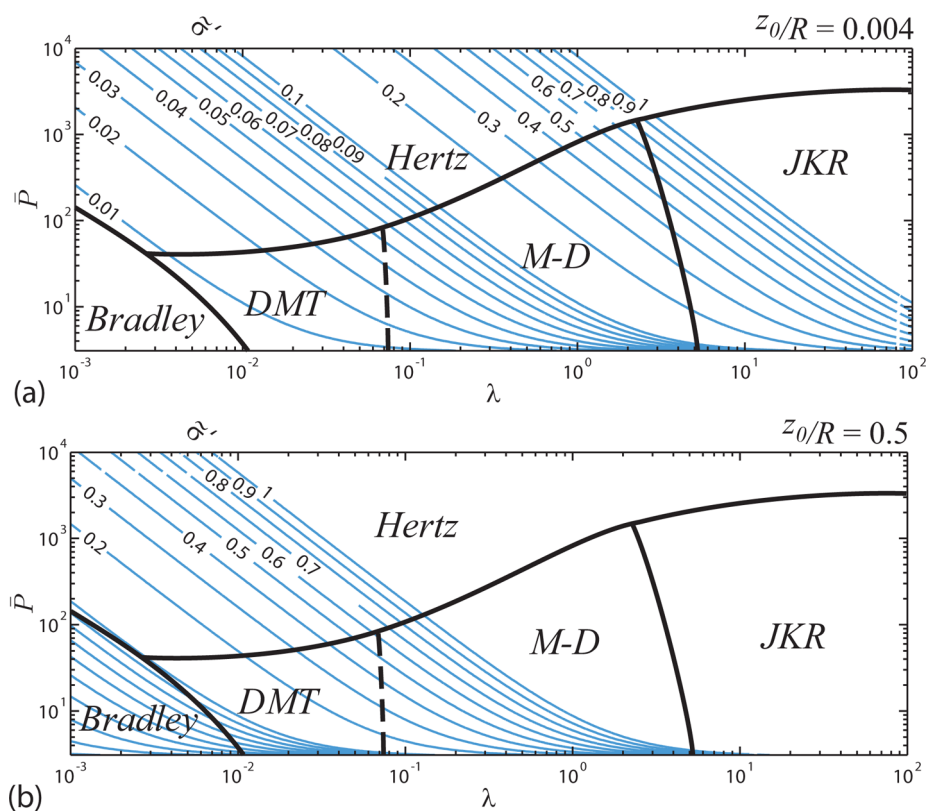
Figure 4. Lines corresponding to constant $\tilde{\sigma}'$ values are plotted over the adhesion map depicted from Figure 5 in the work of Johnson and Greenwood[31] where (a) corresponds to $z_0/R = 0.004$ and (b) to $z_0/R = 0.5$. $\bar{P}$ varies from 3 to 10^4 as $\bar{P}$ cannot be equal or smaller than 3 (see the details in the text). (a) shows that if $\tilde{\sigma}' \leq 0.02$, the DMT contact model holds in all situations. (b) shows that if $\tilde{\sigma}' > 0.5$, the tip−sample contact cannot be described by the DMT model.

The term z_0/R in eq 12 can vary from 0.004 to 0.5 given the typical values reported in the literature for z_0 (0.2−0.5 nm[48]) and typical AFM tip radii (1 to 50 nm). Here, we consider both extreme values to learn about the range of the $\tilde{\sigma}'$ values in which the tip−sample contact cannot be described by the DMT model.

Using eq 12 and the above-mentioned limits, one can superimpose constant $\tilde{\sigma}'$ lines to the adhesion map proposed by Johnson and Greenwood[31] (Figure 4). Figure 4a and b correspond to z_0/R equal to 0.004 and 0.5, respectively. As it can be seen, a wider range of $\tilde{\sigma}'$ values fall into the M-D and JKR regimes in Figure 4a in compare to Figure 4b. By inspecting Figure 4a, it can be concluded that tip−sample contacts with $\tilde{\sigma}'$ values less than or equal to 0.02 are safely in the DMT or Hertz regime, and the use of Figure 3 or 4 is justified. On the other hand, Figure 4b shows that tip−sample contacts with $\tilde{\sigma}'$ values greater than 0.5 cannot be described by the DMT contact model. The shaded area in Figure 3 corresponds to $\tilde{\sigma}'$ values greater than 0.5, for which the stress map is not accurate and should not be used for selecting a proper cantilever or choosing a safe free oscillation amplitude, as the contact stress will be underestimated. Using the adhesion map to determine appropriate contact mechanics model is required for any $\tilde{\sigma}'$ value between approximately 0.02 and 0.5.

EXPERIMENTAL RESULTS

To demonstrate the applicability of the method introduced in the previous section to choose appropriate probe and control the contact stress, several experiments are performed involving three different AFM tip materials or coatings that are commonly used: silicon, DLC, and SiN_x. UNCD[9,49,50] is chosen as the counter surface, as it is hard and wear resistant; consequently, its features do not change significantly during the test. Also, UNCD's sharp and random features can be used for BTR. Table 1 lists the AFM probes used in these experiments, their corresponding location on the DMT-like contact stress map in Figure 3, measured cantilever properties (k, Q, R), the resulting C_{cs} with UNCD as the sample, measured work of adhesion, desired initial σ_{max}, initial $\tilde{\sigma}'$ and its corresponding estimated A_0, determined from Figure 3, and finally the imaging A_{ratio}. The material properties used to calculate C_{cs} and choose a desired initial σ_{max} are listed in Table 2. All the experiments are performed in 15% RH in a mixture of humid air and dry N_2 gas.

One uncoated silicon probe (HQ:NSC19 from MikroMasch) is used to perform four sequential sets of experiments. Each set consisted of 10 AM-AFM scans ($1 \times 1 \, \mu m^2$, 512×512 pixels, 1 Hz scan rate). The first three sets have three different and sequentially increasing initial σ_{max} values. The final set has the same initial maximum compressive stress as the third set, to reevaluate that the required A_0 after the tip radius and C_{cs} have both increased due to wear (see Table 1). Two DLC-coated silicon

TABLE 1. AFM Probes, Their Corresponding Location on the DMT-like Stress Map (Figure 3), Measured Cantilever Physical Properties, Initial C_{cs} with UNCD as the Sample, Measured Work of Adhesion, Desired Initial σ_{max}, Initial $\tilde{\sigma}$ and Its Corresponding Estimated A_0, and A_{ratio} during Imaging

AFM probe	location on the DMT-like stress map (Figure 3)	spring constant (N/m)	res. freq. (=drive freq.) (kHz)	quality factor	initial tip radius (nm)	initial C_{cs} (10^4 nm)	work of adhesion w (J/m²)	targeted initial σ_{max} (GPa)	initial $\tilde{\sigma}$	A_0 (nm)	imaging A_{ratio}
MikroMasch, HQ:NSC19, set 1	red circle #1	0.23 ± 0.01	46.9	74 ± 3	7.8 ± 1.1	3.5 ± 0.9	0.030 ± 0.017	5	0.03	11	0.3
MikroMasch, HQ:NSC19, set 2	red circle #2	0.23 ± 0.01	46.9	74 ± 3	7.3 ± 0.5	3.2 ± 0.5	0.030 ± 0.017	7	0.06	46	0.3
MikroMasch, HQ:NSC19, set 3	out of A_0 range	0.23 ± 0.01	46.9	74 ± 3	7.7 ± 1.3	3.5 ± 1.1	0.030 ± 0.017	9	0.07	109	0.3
MikroMasch, HQ:NSC19, set 4	out of A_0 range	0.23 ± 0.01	46.9	74 ± 3	14 ± 0.5	9.4 ± 1.2	0.030 ± 0.017	9	0.08	317	0.3
nanosensors, PPP-NCHR, 20 nm DLC coating, tip 1	green square #1	42 ± 2	308.6	479 ± 10	21 ± 0.5	2.2 ± 0.3	0.031 ± 0.012	7	0.05	23	0.4
nanosensors, PPP-NCHR, 20 nm DLC coating, tip 2	green square #2	43 ± 2	303.4	498 ± 10	15 ± 1.5	1.3 ± 0.3		11	0.08	50	0.5
MikroMasch, NSC15, 10 nm SiN_x coating, tip 1	magenta star #1	50 ± 2	337.6	663 ± 10	20 ± 2	2.7 ± 0.6	0.036 ± 0.019	9	0.05	23	0.4
MikroMasch, NSC15, 10 nm SiN_x coating, tip 2	magenta star #2	49 ± 2	339.0	648 ± 10	18 ± 0.5	2.3 ± 0.3		12	0.06	50	0.5

TABLE 2. Material Properties Used in the Calculations of C_{cs} and Selecting Desired Initial σ_{max}[a]

	Young's modulus (GPa)	Poisson's ratio	yield/failure strength (GPa)
UNCD	790 ± 30[51]	0.057 ± 0.038[51]	28−51[52]
Si	130	0.28	5.0 −9.0[41]
DLC	150 ± 30[43]	0.3 ± 0.05[44]	7.3−10[42,43]
SiN_x	230 ± 50[53−56]	0.23 ± 0.05[53−56]	8−10,[57] 13[58]

[a] The yield strengths of the DLC coating of the tips here (7.3−10 GPa) are approximated from the hardness of typically 13 GPa reported by K. Sridharan[43] and the empirical equation proposed by Gan et al.[42] for the relationship between the hardness H, Young's modulus E, and yield strength Y of thin film DLC as $H/Y = -0.36 + 0.67 \ln(E/Y)$.

probes (PPP_NCHR from Nanosensors) and two SiN_x-coated probes (NSC15 from MikroMasch) are also tested with different initial σ_{max}. Each test consisted of 10 AM-AFM scans ($1 \times 1 \ \mu m^2$, 512×512 pixels, 2 Hz scan rate).

All the probes tested here have an initial $\tilde{\sigma}'$ between 0.02 and 0.5 (see Table 1); therefore, using the adhesion map and the procedure described in ref 21, the applicability of the DMT contact model can be determined. All cases here are well inside the DMT regime, and Figure 3 and eqs 8 and 9 can be safely used.

By considering the spring constants listed in Table 1, it can be seen that the spring constant of the silicon probe is very small (~0.23 N/m). This is in the range of the spring constant of the probes used typically for contact mode AFM. This soft cantilever is chosen to have a large enough C_{cs} so that its minimum achievable σ_{max} is well below the silicon yield strength, as described before for the selection of appropriate cantilever. C_{cs} values of silicon cantilevers are usually small when used to image a stiff sample such as UNCD because of the sharpness of the tips. The reduced Young's modulus of silicon against UNCD is ~120 GPa, and the nominal tip radius of the silicon tips here is 8 nm.

Figure 5a−d demonstrate the tip radius evolution of the silicon probe imaging a UNCD sample during four consecutive sets of tests. The cumulative number of taps at the end of each set is also noted. Figure 5e−g shows selected topographic images of the UNCD sample obtained with this probe corresponding to the first scan of set 1, the 10th scan of set 2, and the 10th scan of set 4. The initial C_{cs} of set 1 is calculated using a tip radius estimated from BTR of an initial topography image acquired before the first scan. The quality factor and spring constant were also measured experimentally. The initial C_{cs} of sets 2, 3, and 4 are calculated using the tip radius estimated from the BTR of the last topography image of the previous set.

In sets 1 and 2, the initial σ_{max} is 5 and 7 GPa, respectively, which is less than or equal to the silicon failure strength at compression (7.0 GPa, the midrange of 5.0−9.0 GPa). Correspondingly, there is no significant change in the tip radius and quality and spatial resolution of the topographic image. This is impressive considering the 480 million taps (contact formation and breaking) that had occurred by the end of set 2. Increasing the initial σ_{max} to 9 GPa for the test sets 3 and 4, well beyond the yield stress of silicon, resulted in tip wear. This is clearly evident from the increased tip radius (Figure 5c and d) and loss of topography image resolution (Figure 5g). The latter is clearly evident from both the loss of sharpness of the lateral features and reduction of vertical contrast, which can be quantified by comparing the rms roughness in set 1, scan 1 (10.7 nm) and set 4, scan 10 (9.6 nm).

Two different wear regimes can be seen in set 3. During the first five scans the rate of change of the tip radius is small, while the tip radius increases rapidly after the sixth scan and continues to have a high rate of change through the first seven scans of the test set 4. We hypothesize that the top few atomic layers of silicon oxide present on the tip are initially saturated. Then, as wear initiates, surface sites become more reactive as covalent bonds are broken due to wear, leaving behind unsaturated atomic sites on the tip, which can initiate bond formation between the tip and sample atoms. This may correspond to completely removing the oxide[14] or may just involve rendering sites within the oxide more reactive. The presence of water molecules in the environment and the high stress state can also result in a water−silica reaction through water dissociation and chemisorption to the tip surface as described by Zhu et al.[59] and consequently initiation of the wear process.

One other observation that can be made from the change of the tip radius from sixth to 10th scan of set 3 and all of set 4 is the rapid blunting of the tip at the beginning that gradually subsides toward the end. Particularly, in the case of set 4, the tip radius reaches a plateau and does not change any further. This is because of the fact that as the tip radius increases, the contact stresses decrease, resulting in less or no tip wear.[21] A plateau in the wear behavior may also be just beginning to show up at scan 8 of set 3 as well.

Figure 6 shows the tip radius evolution of the DLC- and SiN_x-coated tips with different initial σ_{max}. The cumulative number of taps at the end of test is also noted. The insets are TEM 2D images of each tip's apex before the first and 10th scans. A contamination particle becomes attached to DLC-coated tip 1 sometime between the third (TEM image after the third scan is not shown) and ninth scans. The contaminant is not within or close to the region of the tip apex that interacts with the sample. Therefore, it should not introduce any error in the estimation of the tip radius. The initial C_{cs} of all four cases is calculated using a tip radius estimated from BTR of an initial topography image acquired before the first scan. The quality factor and spring
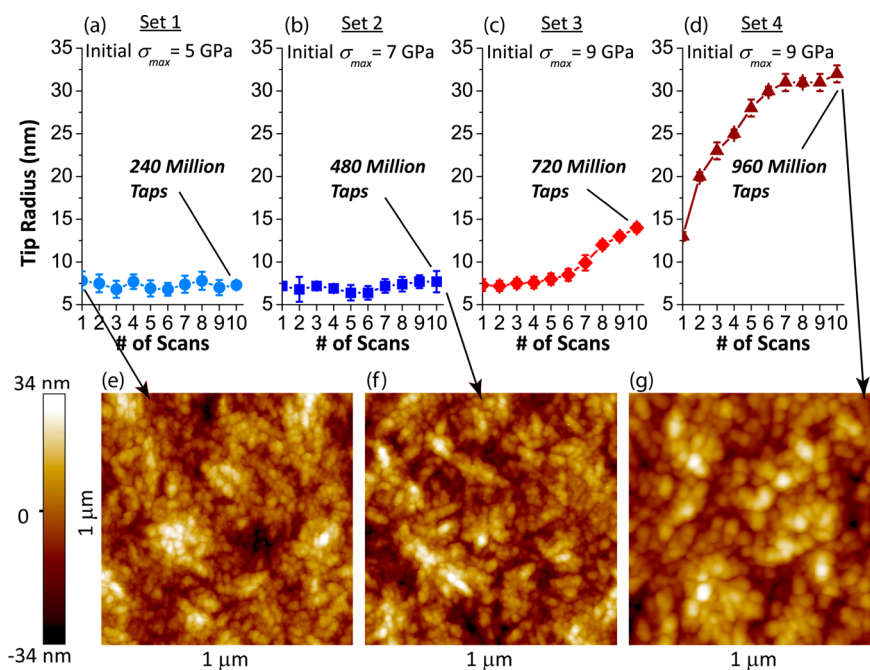
Figure 5. (a–d) Tip radius evolution of a silicon probe (HQ:NSC19 from MikroMasch) imaging a UNCD sample during sets 1–4 using AM-AFM with different initial σ_{max} and the cumulative number of taps at the end of each set. (e) Topographic images of the UNCD sample corresponding to the first scan of set 1; (f) the 10th scan of set 2; and (g) the 10th scan of set 4. The preservation of the tip radius and image resolution is apparent up to the end of test set 2, as the σ_{max} is less than or equal to the silicon failure strength at compression (7.0 GPa). The tip blunting and the loss of image resolution can be seen during the test set 3 and 4, as the initial σ_{max} is 9 GPa, above the silicon yield strength. All relevant parameters for these tests are provided in Tables 1 and 2.
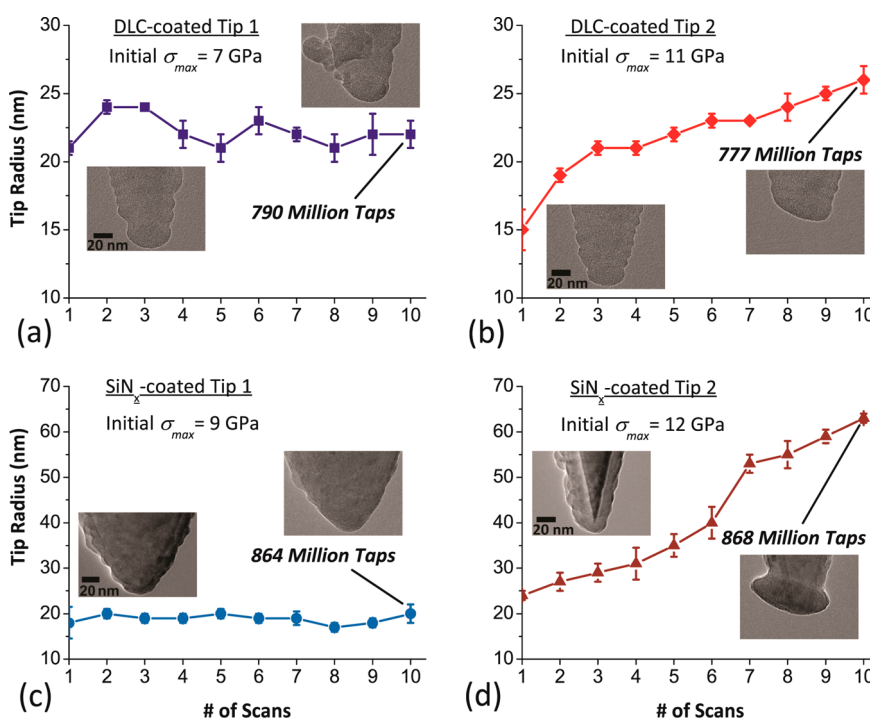

Figure 6. Tip radius evolution of (a) DLC-coated silicon tip 1 with initial σ_{max} of 7 GPa; (b) DLC-coated silicon tip 2 with initial σ_{max} of 11 GPa; (c) SiN$_x$-coated silicon tip 1 with initial σ_{max} of 9 GPa; and (d) SiN$_x$-coated silicon tip 2 with initial σ_{max} of 12 GPa. The cumulative number of taps at the end of each test is also noted. The insets are 2D TEM images of each tip before the first and 10th scans. For both tip materials, the tip radius does not significantly change when the initial σ_{max} is less than or equal to the tip material's yield strength (7.3–10 GPa for DLC, 8–10 for SiN$_x$). When σ_{max} exceeds the tip material's yield strength, tip wear and blunting are significant.

constant are also measured experimentally (Table 1). Similar to the silicon probe, if the initial σ_{max} is below the yield strength of

the tip's material (Figure 6a and c), the tip radius does not change significantly; however, tip blunting happens when the

initial σ_{max} is larger than the yield strength (Figure 6b and d). Differences in the wear behavior of these two materials were reported previously and discussed in more detail by our previous publication.[21]

Note that different values for the yield strength of the SiN$_x$ are provided in Table 2 (8—10 and 13 GPa). The range 8—10 GPa is from a measurement of a powdered α-Si$_3$N$_4$ sample under 9 GPa pressure through the analysis of peak broadening of energy-dispersive diffraction lines.[57] The value of 13 GPa is estimated using Tabor's relationship ($H = CY$ where C is a constraint factor[60]) where the hardness H of an amorphous low-pressure chemical vapor deposited silicon nitride thin film sample was measured using nanoindentation with a cube-corner indenter.[58] The experiments here indicate that the critical failure stress of the SiN$_x$ coating of these tips under these AM-AFM operations is somewhere between 9 and 12 GPa, assuming validity of the continuum DMT model. The values estimated for the failure strength of DLC films also vary significantly in the literature. Depending on the deposition techniques and composition of the tip materials, the failure strength of the AFM tip material and its coating could have significant uncertainty. A series of experiments where the initial σ_{max} is systematically varied, similar to what is done here for the silicon tip (Figure 5), could be performed to estimate a threshold critical stress value for tip failure in AM-AFM operation. This is particularly important when AM-AFM is used for the metrology purposes.

CONCLUSION

We considered the mechanics of tip—sample interactions in AM-AFM. The available techniques and equations to calculate peak repulsive force and contact stress were then presented. Analytical equations applicable for Hertzian- and DMT-like contacts are provided and used to form AM-AFM stress maps. These maps can be used to easily choose an appropriate AM-AFM cantilever and to determine the experimental parameters necessary in AM-AFM to prevent tip/sample wear. The applicability of the method to control the contact stress is examined through a series of AM-AFM experiments with different tip materials and initial maximum compressive stresses imaging a UNCD sample. In all cases, operating with a maximum compressive stress below the yield/failure strength of the tip material prevents tip blunting and preserves the topographic image resolution, while operating with a maximum compressive stress above the yield/failure strength of the tip material leads to significant tip wear.

METHODS

The experiments performed in this study involved the following procedures: (1) pull-off force measurements to determine the work of adhesion between the tip and sample materials; (2) initial assessment of the cantilever physical properties required to calculate the cantilever—sample constant C_{cs} such as quality factor and spring constant using Sader's method[38] and the tip radius using BTR; (3) determination of the inverse optical lever sensitivity (InvOLS) of the cantilever's normal deflection signal to convert the amplitude from measured volts to nanometers using the thermal noise spectrum of the cantilever's flexural vibrations; and (4) keeping the relative humidity of the AFM chamber at 15% through administration of dry N$_2$ gas to the humid air of the chamber. Pull-off force measurements, BTR methodology, and determination of the cantilever's InvOLS are described in detail by Vahdat et al.[21]

The 20 nm DLC coating of the DLC-coated silicon probes was deposited using the plasma immersion ion implantation and deposition process[43] by Dr. K. Sridharan (University of Wisconsin—Madison, Center for Plasma-Aided Manufacturing). The hydrogen content of the DLC film is 41 $\pm$ 2 at. % based on prior hydrogen forward recoil spectroscopy measurements on samples grown using the same method, and approximately 50% to 70% of the carbon structure is in the sp^3 state. Thus, this particular DLC is considered to be an amorphous hydrogenated carbon film (a-C:H).[61] The UNCD film used in these experiments as the sample is deposited on a Si substrate by Advanced Diamond Technologies, Inc. (Aqua 25; Romeoville, IL, USA).

Failure in a Hertzian- or DMT-like Contact. In contact mode AFM, tip wear can be significantly reduced by limiting tip—sample contact stresses.[62,63] Tayebi et al.[62] achieved a low stress state at the tip—sample contact by introducing a thin water layer at the interface and modulating the applied force to have the water layer act as a viscoelastic material reducing the contact stress. The write-read resolution of a platinum—iridium tip in the probe-based memory device did not change after 5 km of sliding on a smooth ferroelectric film. Also, Lantz et al.[63] achieved low wear by modulating electrostatic forces between the tip and sample (by applying sinusoidal voltage to the tip and sample), resulting in a very low friction. They showed experimentally that this technique could almost eliminate wear of a silicon tip sliding over a polymer film over a distance of 750 m. An approach to prevent tip/sample wear by controlling the contact stress in AM-AFM is presented here.

We choose the failure criterion in AM-AFM to correspond to the case where the maximum compressive contact stress experienced during AM-AFM cyclic operation is equal to the yield stress (or other chosen failure stress) of the tip or sample material, whichever is smaller. Here, we discuss the motivation for selecting this criterion in a Hertzian or DMT contact. To prevent tip/sample wear, we consider the locations in the tip and sample, or at the interface between them, that correspond to the maximum stress components. Figure 7 shows the stress distributions in a Hertzian contact normalized to the mean contact stress. In the top graph, the normalized principal stresses at the interface, inside and outside of the contact, are plotted as a function of the radial coordinate r normalized by the contact radius a. In the bottom graph, the normalized principal stresses and the absolute maximum shear stress along the central axis of symmetry ($r = 0$) below the interface are plotted as a function of the vertical coordinate z normalized by a. The locations of the maximum values of the tensile, compressive, and shear stress components are indicated with arrows. The maximum compressive stress is at the interface at the center of the contact, the maximum tensile stress is at the interface at the periphery of the contact, and the maximum shear stress is below the interface along the central axis of the contact (the exact location depends on Poisson's ratios of the tip and sample).[27]

Any of these stress components could be the critical ones that lead to failure initiating at their respective locations; however, different materials have different strength limits for each of these stress components. For example, brittle materials have much lower tensile strengths than compressive strengths, and so the largest tensile stress may determine failure, while ductile materials usually fail when one exceeds a critical shear stress. As seen in Figure 7, the magnitude of the maximum compressive stress significantly exceeds that of the maximum tensile and shear stress components. Therefore, we can design the failure criterion conservatively by defining it to be that failure occurs when the maximum compressive stress in the contact reaches the smallest yield or failure strength of the material.
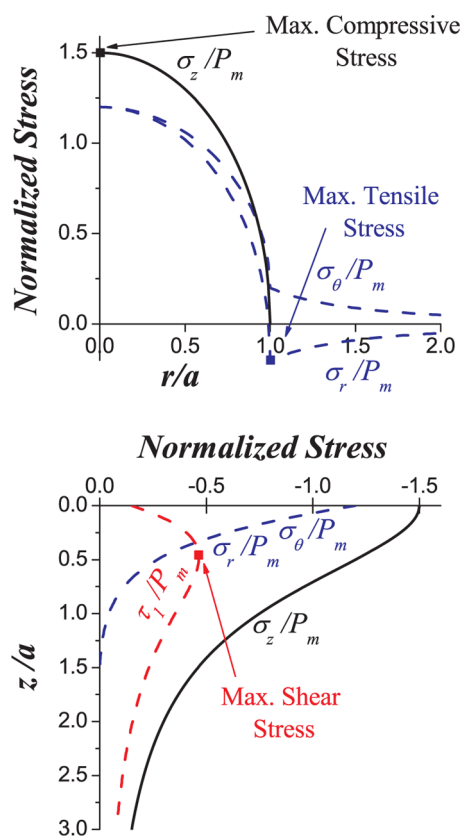
Figure 7. Stress distributions at the surface and along the axis of symmetry caused by Hertz pressure acting on a circular area with radius *a*. All the stress components are normalized by mean contact compressive stress P_m. This image is adapted from Figure 4.3 of the book *Contact Mechanics* by K. L. Johnson using eqs 3.43*a* to 3.45*b* assuming a Poisson's ratio of 0.3.[27]

If failure in the tip or sample material occurs by a combination of stress components, one needs to consider an appropriate yield criterion for a given material. There are multiple yield criteria; these are in fact all empirically based, and considering them all comprehensively is beyond the scope of this work. Here, we consider a simple and popular failure criterion, the von Mises yield criterion, which applies to ductile materials that fail primarily through shear stress-induced plastic flow of dislocations; such materials show similar behavior in both tension and compression. Then, we discuss how this criterion can be related to the maximum compressive stress and whether or not our criterion still acts as an upper bound. As mentioned above, in a Hertzian contact, the maximum shear stress occurs below the surface at the center of the contact. If we assume a Poisson's ratio of 0.3, which is equal or close to most of the materials' Poisson's ratio, this location is at $z = 0.48a$ along the z-axis below the interface at the center of contact, where *a* is the contact radius.[27] If we express the von Mises yield criterion[64] based on the principal stresses of the Hertzian contact, yield happens when the following is satisfied:

$$(\sigma_r - \sigma_\theta)^2 + (\sigma_\theta - \sigma_z)^2 + (\sigma_z - \sigma_r)^2 = 2Y^2 \qquad (13)$$

where σ_r, σ_θ, and σ_z are principal radial, tangential, and normal Hertzian stresses along the z-axis of the contact, and *Y* is the yield strength of the tip or sample material. By inserting the expressions for the Hertzian principal stresses at $z = 0.48a$ into eq 13, the von Mises criterion reduces to

$$\sigma_{max} = 1.613Y \qquad (14)$$

where σ_{max} is the maximum compressive stress. This means that if the maximum compressive stress exceeds 1.613 times yield

stress of a material, it should fail at a distance equal to $0.48a$ below the surface. If we assume a more conservative yield criterion such as Tresca,[64] we get similar results for the Hertzian contact. This is because in the Hertzian contact $\sigma_r - \sigma_\theta = 0$ and $(\sigma_\theta - \sigma_z)^2 = (\sigma_z - \sigma_r)^2$; therefore, the von Mises reduces to Tresca criterion. Again, if σ_{max} is chosen to be less than the tip or sample yield/failure strength, a conservative upper-bound limit is set, which in turn should be safe for the materials for which their failure cannot be accurately determined through von Mises criterion.

Because of the high frequency of the cantilever oscillation and consequently the tip–sample interaction, which can be on the order of hundreds of thousands of tip–sample contacts per second, the effect of any gradual process such as atom-by-atom removal, dislocation movement, or fatigue can accumulate substantially. The rate of atom loss in an atom-by-atom removal process can be exponentially dependent on the contact stresses.[12,14,65] However, this dependence can vary for different tip and sample material pairs and environmental conditions, which can alter the nature of the chemical reactions at the contact. Therefore, proposing a specific criterion to prevent atom-by-atom removal is not possible at this time. Rather, the best available approach is simply to reduce the tip sample contact stress beyond a safe target value. As well, there is insufficient knowledge regarding nanoscale fatigue as a result of cyclic loading to establish a reliable criterion to prevent or reduce its consequences. Again, using a lower stress value as the critical stress for the failure is a reasonable prescription.

Conflict of Interest: The authors declare no competing financial interest.

REFERENCES AND NOTES

1. Prater, C. B.; Strausser, Y. E. Tapping Mode AFM-Applications to Semiconductors. In *Proceedings of the 5th International Conference on Defect Recognition and Image Processing in Semiconductors and Devices*; Jiménez, J., Ed.; Santander: Spain, **1993**; pp 69–72.
2. García, R.; Perez, R. Dynamic Atomic Force Microscopy Methods. *Surf. Sci. Rep.* **2002**, *47*, 197–301.
3. Xu, X.; Carrasco, C.; de Pablo, P. J.; Gomez-Herrero, J.; Raman, A. Unmasking Imaging Forces on Soft Biological Samples in Liquids When Using Dynamic Atomic Force Microscopy: A Case Study on Viral Capsids. *Biophys. J.* **2008**, *95*, 2520–2528.
4. Liu, Z.; Li, Z.; Wei, G.; Song, Y.; Wang, L. I.; Sun, L. Manipulation, Dissection, and Lithography Using Modified Tapping Mode Atomic Force Microscope. *Microsc. Res. Tech.* **2006**, *69*, 998–1004.
5. Wang, Y.; Hong, X.; Zeng, J.; Liu, B.; Guo, B.; Yan, H. AFM Tip Hammering Nanolithography. *Small* **2009**, *5*, 477–483.
6. Paolicelli, G.; Mougin, K.; Vanossi, A.; Valeri, S. Adhesion Detachment and Movement of Gold Nanoclusters Induced by Dynamic Atomic Force Microscopy. *J. Phys.: Condens. Matter* **2008**, *20*, 354011-1–354011-6.
7. Martínez, N. F.; Kamiński, W.; Gómez, C. J.; Albonetti, C.; Biscarini, F.; Pérez, R.; García, R. Molecular Scale Energy Dissipation in Oligothiophene Monolayers Measured by Dynamic Force Microscopy. *Nanotechnology* **2009**, *20*, 434021-1–434021-7.
8. Dietz, C.; Zerson, M.; Riesch, C.; Franke, M.; Magerle, R. Surface Properties of Elastomeric Polypropylenes Studied with Atomic Force Microscopy. *Macromolecules* **2008**, *41*, 9259–9266.
9. Liu, J.; Notbohm, J. K.; Carpick, R. W.; Turner, K. T. Method for Characterizing Nanoscale Wear of Atomic Force Microscope Tips. *ACS Nano* **2010**, *4*, 3763–3772.

10. Chung, K.-H.; Lee, Y.-H.; Kim, D.-E. Characteristics of Fracture during the Approach Process and Wear Mechanism of a Silicon AFM Tip. *Ultramicroscopy* **2005**, *102*, 161–171.

11. Merkle, A. P.; Marks, L. D. Liquid-Like Tribology of Gold Studied by *in Situ* TEM. *Wear* **2008**, *265*, 1864–1869.

12. Gotsmann, B.; Lantz, M. Atomistic Wear in a Single Asperity Sliding Contact. *Phys. Rev. Lett.* **2008**, *101*, 125501-1–125501-4.

13. Jacobs, T. D. B.; Gotsmann, B.; Lantz, M. A.; Carpick, R. W. On the Application of Transition State Theory to Atomic-Scale Wear. *Tribol. Lett.* **2010**, *39*, 257–271.

14. Jacobs, T. D. B.; Carpick, R. W. Nanoscale Wear as a Stress-Assisted Chemical Reaction. *Nat. Nanotechnol.* **2013**, *8*, 108–112.

15. Hölscher, H.; Schwarz, U. D. Theory of Amplitude Modulation Atomic Force Microscopy with and without Q-Control. *Int. J. Nonlinear Mech.* **2007**, *42*, 608–625.

16. García, R.; Paulo, A. S. Attractive and Repulsive Tip-Sample Interaction Regimes in Tapping-Mode Atomic Force Microscopy. *Phys. Rev. B* **1999**, *60*, 4961–4967.

17. Schröter, K.; Petzold, A.; Henze, T.; Thurn-Albrecht, T. Quantitative Analysis of Scanning Force Microscopy Data Using Harmonic Models. *Macromolecules* **2009**, *42*, 1114–1124.

18. Hu, S.; Raman, A. Inverting Amplitude and Phase to Reconstruct Tip-Sample Interaction Forces in Tapping Mode Atomic Force Microscopy. *Nanotechnology* **2008**, *19*, 375704-1–375704-11.

19. Katan, A. J.; Es, M. H.; van Oosterkamp, T. H. Quantitative Force versus Distance Measurements in Amplitude Modulation AFM: A Novel Force Inversion Technique. *Nanotechnology* **2009**, *20*, 165703-1–165703-9.

20. Hu, S.; Raman, A. Analytical Formulas and Scaling Laws for Peak Interaction Forces in Dynamic Atomic Force Microscopy. *Appl. Phys. Lett.* **2007**, *91*, 123106-1–123106-3.

21. Vahdat, V.; Grierson, D. S.; Turner, K. T.; Carpick, R. W. Mechanics of Interaction and Atomic-Scale Wear of Amplitude Modulation Atomic Force Microscopy Probes. *ACS Nano* **2013**, *7*, 3221–3235.

22. Tello, M.; Paulo, A. S.; Rodríguez, T. R.; Blanco, M. C.; García, R. Imaging Cobalt Nanoparticles by Amplitude Modulation Atomic Force Microscopy: Comparison between Low and High Amplitude Solutions. *Ultramicroscopy* **2003**, *97*, 171–175.

23. San Paulo, A.; García, R. High-Resolution Imaging of Antibodies by Tapping-Mode Atomic Force Microscopy: Attractive and Repulsive Tip-Sample Interaction Regimes. *Biophys. J.* **2000**, *78*, 1599–1605.

24. Thormann, E.; Pettersson, T.; Kettle, J.; Claesson, P. M. Probing Material Properties of Polymeric Surface Layers with Tapping Mode AFM: Which Cantilever Spring Constant, Tapping Amplitude and Amplitude Set Point Gives Good Image Contrast and Minimal Surface Damage? *Ultramicroscopy* **2010**, *110*, 313–319.

25. Su, C.; Huang, L.; Kjoller, K.; Babcock, K. Studies of Tip Wear Processes in Tapping Mode™ Atomic Force Microscopy. *Ultramicroscopy* **2003**, *97*, 135–144.

26. Chen, L.; Cheung, C. L.; Ashby, P. D.; Lieber, C. M. Single-Walled Carbon Nanotube AFM Probes: Optimal Imaging Resolution of Nanoclusters and Biomolecules in Ambient and Fluid Environments. *Nano Lett.* **2004**, *4*, 1725–1731.

27. Johnson, K. L. *Contact Mechanics*; Cambridge University Press, 1985.

28. Derjaguin, B.; Muller, V.; Toporov, Y. Effect of Contact Deformations on the Adhesion of Particles. *J. Colloid Interface Sci.* **1975**, *53*, 314–326.

29. Melcher, J.; Kiracofe, D.; Hu, S.; Raman, A. *VEDA 2.0* (Virtual Environment for Dynamic AFM), 2012.

30. Grierson, D. S.; Flater, E. E.; Carpick, R. W. Accounting for the JKR−DMT Transition in Adhesion and Friction Measurements with Atomic Force Microscopy. *J. Adhes. Sci. Technol.* **2005**, *19*, 291–311.

31. Johnson, K. L.; Greenwood, J. A. An Adhesion Map for the Contact of Elastic Spheres. *J. Colloid Interface Sci.* **1997**, *192*, 326–333.

32. Szoszkiewicz, R.; Riedo, E. Nucleation Time of Nanoscale Water Bridges. *Phys. Rev. Lett.* **2005**, *95*, 135502-1–135502-4.

33. Restagno, F.; Bocquet, L.; Biben, T. Metastability and Nucleation in Capillary Condensation. *Phys. Rev. Lett.* **2000**, *84*, 2433–2436.

34. Sahagún, E.; García-Mochales, P.; Sacha, G.; Sáenz, J. Energy Dissipation Due to Capillary Interactions: Hydrophobicity Maps in Force Microscopy. *Phys. Rev. Lett.* **2007**, *98*, 176106-1–176106-4.

35. Zitzler, L.; Herminghaus, S.; Mugele, F. Capillary Forces in Tapping Mode Atomic Force Microscopy. *Phys. Rev. B* **2002**, *66*, 155436-1–155436-8.

36. Hu, S. *Nonlinear Dynamics and Force Spectroscopy in Dynamic Atomic Force Microscopy*, Ph.D. Thesis, Purdue University, West Lafayette, IN, 2007, pp 74−101.

37. Hutter, J. L.; Bechhoefer, J. Calibration of Atomic-Force Microscope Tips. *Rev. Sci. Instrum.* **1993**, *64*, 1868–1873.

38. Sader, J. E.; Chon, J. W. M.; Mulvaney, P. Calibration of Rectangular Atomic Force Microscope Cantilevers. *Rev. Sci. Instrum.* **1999**, *70*, 3967–3969.

39. Brandrup, J.; Immergut, E. H.; Grulke, E. A. *Polymer Hand-Book*, 4th ed.; Wiley: New York, NY, 1999.

40. Klein, C. A.; Cardinale, G. F. Young's Modulus and Poisson's Ratio of CVD Diamond. *Diam. Relat. Mater.* **1993**, *2*, 918–923.

41. Howatson, A. M.; Lund, P. G.; Todd, J. D. *Engineering Tables and Data*, 2nd ed.; Springer, 1991.

42. Gan, Z.; Zhang, Y.; Yu, G.; Tan, C.; Lau, S.; Tay, B. Intrinsic Mechanical Properties of Diamond-Like Carbon Thin Films Deposited by Filtered Cathodic Vacuum Arc. *J. Appl. Phys.* **2004**, *95*, 3509–3515.

43. Bares, J. A.; Sumant, A. V.; Grierson, D. S.; Carpick, R. W.; Sridharan, K. Small Amplitude Reciprocating Wear Performance of Diamond-Like Carbon Films: Dependence of Film Composition and Counterface Material. *Tribol. Lett.* **2007**, *27*, 79–88.

44. Marques, F. C.; Lacerda, R. G.; Champi, A.; Stolojan, V.; Cox, D. C.; Silva, S. R. P. Thermal Expansion Coefficient of Hydrogenated Amorphous Carbon. *Appl. Phys. Lett.* **2003**, *83*, 3099–3101.

45. Olliges, S.; Frank, S.; Gruber, P. a.; Auzelyte, V.; Solak, H.; Spolenak, R. Thermo Mechanical Properties and Plastic Deformation of Gold Nanolines and Gold Thin Films. *Mater. Sci. Eng., A* **2011**, *528*, 6203–6209.

46. Maugis, D. Adhesion of Spheres: The JKR-DMT Transition Using a Dugdale Model. *J. Colloid Interface Sci.* **1992**, *150*, 243–269.

47. Johnson, K.; Kendall, K.; Roberts, A. D. Surface Energy and the Contact of Elastic Solids. *Proc. R. Soc. London A* **1971**, *324*, 301−313.

48. Grierson, D. S.; Liu, J.; Carpick, R. W.; Turner, K. T. Adhesion of Nanoscale Asperities with Power-Law Profiles. *J. Mech. Phys. Solids* **2013**, *61*, 597–610.

49. Liu, J.; Grierson, D. S.; Moldovan, N.; Notbohm, J.; Li, S.; Jaroenapibal, P.; O'Connor, S. D.; Sumant, a V; Neelakantan, N.; Carlisle, J. A.; *et al.* Preventing Nanoscale Wear of Atomic Force Microscopy Tips through the Use of Monolithic Ultrananocrystalline Diamond Probes. *Small* **2010**, *6*, 1140–1149.

50. Fletcher, P. C.; Felts, J. R.; Dai, Z.; Jacobs, T. D.; Zeng, H.; Lee, W.; Sheehan, P. E.; Carlisle, K. J. A.; Carpick, R. W.; King, W. P. Wear-Resistant Diamond Nanoprobe Tips with Integrated Silicon Heater for Tip-Based Nanomanufacturing. *ACS Nano* **2010**, *4*, 3338–3344.

51. Adiga, V.; Sumant, A.; Suresh, S.; Gudeman, C.; Auciello, O.; Carlisle, J.; Carpick, R. Mechanical Stiffness and Dissipation in Ultrananocrystalline Diamond Microresonators. *Phys. Rev. B* **2009**, *79*, 245403-1–245403-8.

52. Mo, Y.; Stone, D.; Szlufarska, I. Strength of Ultrananocrystalline Diamond Controlled by Friction of Buried Interfaces. *J. Phys. D: Appl. Phys* **2011**, *44*, 405401-1–405401-10.

53. Khan, A.; Philip, J.; Hess, P. Young's Modulus of Silicon Nitride Used in Scanning Force Microscope Cantilevers. *J. Appl. Phys.* **2004**, *95*, 1667–1672.

54. Dai, C.-L.; Chang, Y.-M. A Resonant Method for Determining Mechanical Properties of Si_3N_4 and SiO_2 Thin Films. *Mater. Lett.* **2007**, *61*, 3089–3092.

55. Chuang, W.; Luger, T.; Fettig, R. K.; Ghodssi, R. Mechanical Property Characterization of LPCVD Silicon Nitride Thin Films at Cryogenic Temperatures. *J. Microelectromech. Syst.* **2004**, *13*, 870–879.

56. Edwards, R. L.; Coles, G.; Sharpe, W. N. Comparison of Tensile and Bulge Tests for Thin-Film Silicon Nitride. *Exp. Mech.* **2004**, *44*, 49–54.

57. Qian, J.; Pantea, C.; Zhang, J.; Daemen, L. L.; Zhao, Y.; Tang, M.; Uchida, T.; Wang, Y. Yield Strength of Alpha-Silicon Nitride at High Pressure and High Temperature. *J. Am. Ceram. Soc.* **2005**, *88*, 903–906.

58. Merle, B.; Göken, M. Fracture Toughness of Silicon Nitride Thin Films of Different Thicknesses As Measured by Bulge Tests. *Acta Mater.* **2011**, *59*, 1772–1779.

59. Zhu, T.; Li, J.; Lin, X.; Yip, S. Stress-Dependent Molecular Pathways of Silica−Water Reaction. *J. Mech. Phys. Solids* **2005**, *53*, 1597–1623.

60. Tabor, D. *The Hardness of Metals*; Oxford University Press: Oxford, 1951.

61. Robertson, J. Diamond-Like Amorphous Carbon. *Mater. Sci. Eng. R Rep.* **2002**, *37*, 129–281.

62. Tayebi, N.; Zhang, Y.; Chen, R. J.; Tran, Q.; Chen, R.; Nishi, Y.; Ma, Q.; Rao, V. An Ultraclean Tip-Wear Reduction Scheme for Ultrahigh Density Scanning Probe-Based Data Storage. *ACS Nano* **2010**, *4*, 5713–5720.

63. Lantz, M. A.; Wiesmann, D.; Gotsmann, B. Dynamic Superlubricity and the Elimination of Wear on the Nanoscale. *Nat. Nanotechnol.* **2009**, *4*, 586–591.

64. Boresi, A. P.; Schmidt, R. J. Inelastic Material Behavior. In *Advanced Mechanics of Materials*; John Wiley & Sons, Inc.: New York, NY, 2003.

65. Bhaskaran, H.; Gotsmann, B.; Sebastian, A.; Drechsler, U.; Lantz, M. A.; Despont, M.; Jaroenapibal, P.; Carpick, R. W.; Chen, Y.; Sridharan, K. Ultra-Low Nanoscale Wear through Atom-by-Atom Attrition in Silicon-Containing Diamond-Like Carbon. *Nat. Nanotechnol.* **2010**, *5*, 181–185.